

Simulation of Rayleigh-Bénard convection using lattice Boltzmann method

Xiaowen Shan

USAF Phillips Laboratory, Hanscom AFB, Massachusetts 01731

Theoretical Division, Los Alamos National Laboratory, Los Alamos, New Mexico 87545

(December 16, 2013)

Abstract

Rayleigh-Bénard convection is numerically simulated in two- and three-dimensions using a recently developed two-component lattice Boltzmann equation (LBE) method. The density field of the second component, which evolves according to the advection-diffusion equation of a passive-scalar, is used to simulate the temperature field. A body force proportional to the temperature is applied, and the system satisfies the Boussinesq equation except for a slight compressibility. A no-slip, isothermal boundary condition is imposed in the vertical direction, and periodic boundary conditions are used in horizontal directions. The critical Rayleigh number for the onset of the Rayleigh-Bénard convection agrees with the theoretical prediction. As the Rayleigh number is increased higher, the steady two-dimensional convection rolls become unstable. The wavy instability and aperiodic motion observed, as well as the Nusselt number as a function of the Rayleigh number, are in good agreement with experimental observations and theoretical predictions. The LBE model is found to be efficient, accurate, and numerically stable for the simulation of fluid flows with heat and mass transfer.

Typeset using REVTeX

I. INTRODUCTION

Recently the lattice Boltzmann equation (LBE) method has been developed as a new computational fluid dynamics (CFD) method. This method originated from a boolean fluid model known as the Lattice Gas Automata (LGA) [1,2] which simulates the motion of fluids by particles moving and colliding on a regular lattice. The averaged fluid variables, such as the density and velocity, were shown to satisfy equations similar to the Navier-Stokes equations. The LBE method improves this idea by following only the ensemble-averaged distribution functions, therefore eliminating the time-consuming statistical average step in the original LGA [3]. Simplified collision models were later used in place of the collision operator derived from the LGA to improve both the computational efficiency and the accuracy. Most noteworthy, the simple collision model of Bhatnagar, Gross, and Krook [4] was applied to the lattice Boltzmann equation, yielding the so called lattice BGK model [5,6]. The additional flexibility in this approach allows the removal of the artifacts of the LGA, specifically the lack of Galilean invariance and the velocity dependent pressure. This method was found numerically to be at least as stable, accurate and computationally efficient as traditional CFD methods for simulation of simple single-phase incompressible flows [7–9]. More importantly, since fluid motion is simulated at the level of the distribution functions, the microscopic physics of the fluid particles can be incorporated easily like in other particle methods. Many complex fluid phenomena due to interparticle interactions, such as capillary phenomena, multiple phase flows, and non-linear diffusion, can be simulated naturally [10–12].

In most LBE models so far, only mass and momentum conservation is implemented. The macroscopic equations of these models correspond to the Navier-Stokes equation with an ideal-gas equation of state and a constant temperature. However it is important and sometimes critical to have the capability of simulating thermal effects simultaneously with the fluid flows. Obviously the temperature distribution in a flow field is of central interest in heat transfer problems. In most geophysical flows, the temperature difference is the driving mechanism of the motion of the fluid. More importantly, when part of the fluid system undergoes phase transition, as in the boiling and evaporation processes, the evolution of the temperature field is directly coupled with the fluid

dynamics. Since the LBE method has the most advantage in the simulation of complex fluids with multiple phases and phase transitions, it is necessary to develop the capability of simulating thermodynamics with the LBE method.

In general, the simulation of thermal systems by the LBE method has not achieved the same success as that of iso-thermal flows. Theoretically, a LBE model with energy conservation can be constructed [13,14] to yield a temperature evolution equation at the macroscopic level. However, the model so obtained suffers from severe numerical instability [15], especially in three-dimensions (3D). Additional stabilization procedures have to be invoked to achieve stability comparable to that of conventional CFD methods, *e.g.*, finite difference schemes. Moreover, when interparticle forces are included as in the multi-phase models, the energy conservation is further complicated by the potential part of the internal energy. For these reasons constructing a practically usable non-ideal-gas LBE model with energy conservation is difficult if not impossible. Nevertheless, in many circumstances where the viscous and compressive heating effects can be neglected (small Brinkman number limit), the temperature field is passively advected by the fluid flow and obeys a much simpler passive-scalar equation. This same equation also governs the diffusion of each individual component in a fluid mixture. By taking advantage of this formal analogy between heat and mass transfer, we can simulate the temperature field as an additional component of the fluid system. Early two-component LGA model [16] exhibited qualitative features of thermal convections. In a previously developed multiple component LBE model [17], we have shown that the evolution of the concentration fields is Galilean invariant and obeys Fick's law. The diffusivity is independent of the viscosity, allowing a changeable Schmidt number (or Prandtl number in the terminology of heat transfer). This model does not implement energy conservation and therefore has the same stability as the non-thermal LBE models and other conventional CFD methods. By adding one more component, the computation efficiency, either memory-wise or time-wise, is not compromised compared with the approach of direct implementation of energy conservation because fewer speeds are required for each component.

In this paper, we present the simulation of the Rayleigh-Bénard convection (RBC) as an example. Due to its simplicity and the richness of the phenomena, this problem has been extensively

studied both theoretically and experimentally [18–22] and serves as an excellent benchmark problem for numerical schemes because detailed results are available for comparison with numerical computations. In section II, we briefly review the multiple component LBE model and then formulated it for the simulation of the Boussinesq equation. The implementation of the isothermal no-slip boundary condition is also discussed. In section III, simulation results are presented and compared with theoretical and experimental results. The limitation and some further extensions of this method are discussed in section IV.

II. NUMERICAL METHOD

The following single component lattice Boltzmann equation with BGK collision term describes the evolution of the distribution function $n_a(\mathbf{x}, t)$ in space \mathbf{x} and time t .

$$n_a(\mathbf{x} + \mathbf{e}_a, t + 1) - n_a(\mathbf{x}, t) = -\frac{1}{\tau} \left[n_a(\mathbf{x}, t) - n_a^{(\text{eq})}(\mathbf{x}, t) \right], \quad a = 1, \dots, b \quad (1)$$

The set of b vectors $\{\mathbf{e}_a; a = 1, \dots, b\}$ pointing from each lattice site to its neighboring sites forms the discretized velocity space of the distribution function. The macroscopic number density, $n(\mathbf{x}, t)$, and velocity, $\mathbf{u}(\mathbf{x}, t)$, of the fluid are obtained from n_a as $n = \sum_a n_a$ and $n\mathbf{u} = \sum_a n_a \mathbf{e}_a$. Eq. (1) represents the relaxation of the distribution function to its equilibrium value, $n_a^{(\text{eq})}$, which is a function of n and \mathbf{u} only. The choice of $n_a^{(\text{eq})}$ has to ensure that the macroscopic fluid equation obtained from Eq. (1) by Chapman-Enskog calculation [23] agrees with the Navier-Stokes equations. The functional form of $n_a^{(\text{eq})}$ depends on the structure of the lattice and is usually not uniquely determined. For square and cubic lattices in 2D and 3D, the following form of $n_a^{(\text{eq})}$ was shown to yield Navier-Stokes equations by Qian *et al.* [6]:

$$n_a^{(\text{eq})} = w_a n \left[1 + 3\mathbf{e}_a \cdot \mathbf{u} + \frac{9}{2}(\mathbf{e}_a \cdot \mathbf{u})^2 - \frac{3\mathbf{u} \cdot \mathbf{u}}{2} \right]. \quad (2)$$

Here w_a is a function of $|\mathbf{e}_a|$ and depends on the number of speeds included in the model. In the present work, 9 and 15 velocities are used in 2D and 3D computation respectively. The w_a 's were given as 4/9, 1/9, and 1/36 for $|\mathbf{e}_a| = 0, 1, \sqrt{2}$ in 2D and 2/9, 1/9, and 1/72 for $|\mathbf{e}_a| = 0, 1, \sqrt{3}$

in 3D [6]. It can be easily verify that the 2D distribution function is a degenerate case of the 3D version if the flow is two-dimensional.

A. Multiple component LBE model

The multiple component LBE model with interparticle interaction [10] was originally developed for simulation of multi-phase flows and phase transitions. The components can be miscible or partially immiscible depending on the strength of the interaction. When the interaction is weak, or in a single phase region of a multiphase system, this model can be used to simulate diffusion due to various driving mechanisms [24]. In this model, the distribution function of each component evolves according to Eq. (1). The same form of the equilibrium distribution function given by Eq. (2) is used for all the components except that n and \mathbf{u} are calculated separately for each component. In the absence of any interaction and external forces, the distribution functions of all the components were assumed to have a common velocity, \mathbf{u}' . The conservation of the total momentum at each collision requires that

$$\mathbf{u}' = \sum_{\sigma=1}^S \frac{m_{\sigma} n_{\sigma} \mathbf{u}_{\sigma}}{\tau_{\sigma}} / \sum_{\sigma=1}^S \frac{m_{\sigma} n_{\sigma}}{\tau_{\sigma}}, \quad (3)$$

where S is the number of components in the system; m_{σ} , τ_{σ} and $n_{\sigma} = \sum_a n_a^{\sigma}$ are the molecular mass, the relaxation time, the number density of the component σ respectively, and $m_{\sigma} n_{\sigma} \mathbf{u}_{\sigma} = m_{\sigma} \sum_a n_a^{\sigma} \mathbf{e}_a$ is the momentum of component σ calculated from its distribution function n_a^{σ} . When the force \mathbf{F}_{σ} is applied to component σ , the momentum has to be incremented correspondingly. This was done by replacing \mathbf{u} in Eq. (2) with $\mathbf{u}' + \tau_{\sigma} \mathbf{F}_{\sigma} / \rho_{\sigma}$. The force \mathbf{F}_{σ} in general includes both interparticle forces and external forces. For nearest-neighbor interaction, the following form of the interparticle force was proposed as it conserves the total momentum of the system and yields an adjustable equation of state at the macroscopic level:

$$\mathbf{F}_{\sigma} = -\psi_{\sigma} \sum_{\bar{\sigma}} \mathcal{G}_{\sigma\bar{\sigma}} \sum_a \psi_{\bar{\sigma}}(\mathbf{x} + \mathbf{e}_a) \mathbf{e}_a, \quad (4)$$

where ψ_{σ} is an arbitrary function of the number density of the σ th component.

In the most general multiple component LBE model with interparticle interaction and external forces, there are three types of diffusions due to different driving mechanisms [24]. They are *ordinary diffusion*, *pressure diffusion* and *forced diffusion*. With the equilibrium distribution functions given by Eq. (2), the pressure diffusion does not appear; if a common acceleration is applied to all the components, namely $\mathbf{F}_\sigma = \rho_\sigma \mathbf{g}$, forced diffusion is also absent. The only type of diffusion left is the ordinary diffusion due to concentration gradients which obeys Fick's law. In addition, a component, *e.g.* component S , can be made to behave as a passive-scalar by setting its molecular mass to zero together with its interaction with all the other components, namely $m_S \rightarrow 0$ and $\mathcal{G}_{\sigma S} \rightarrow 0$ for $\sigma = 1, \dots, S-1$. This component will not contribute to the total momentum of the mixture. It is simply advected "passively" and diffuses into the main flow, having no effect on the flow.

For the study of the RBC, we employ a two-component system; component 1 represents the motion of the fluid and component 2 simulates a passive temperature field. The distribution functions of the two components evolve according to Eqs. (1) and (2), with \mathbf{u} in Eq. (2) being replaced by $\mathbf{u}_1 + \tau_\sigma \mathbf{g}$ for both components. Since the molecular masses of the two components no longer appear in the dynamic equations, they are set to unity. The density and the fluid velocity are calculated from the distribution function of component 1 as $\rho = \sum_a n_a^1$ and $\mathbf{u} = \mathbf{u}_1 + \mathbf{g}/2$, (c.f. Ref. [17]). They satisfy the following equations

$$\frac{\partial \rho}{\partial t} + \nabla \cdot (\rho \mathbf{u}) = 0 \quad (5)$$

$$\frac{\partial \mathbf{u}}{\partial t} + \mathbf{u} \cdot \nabla \mathbf{u} = -\frac{\nabla p}{\rho} + \nu \nabla^2 \mathbf{u} + \mathbf{g}. \quad (6)$$

where the pressure p is related to ρ by the equation of state $p = \frac{1}{3}\rho + \frac{3}{2}\mathcal{G}_{11}\psi^2(\rho)$. In the simulation of RBC, it is sufficient to set $\mathcal{G}_{11} = 0$. The kinematic viscosity ν is given by

$$\nu = \frac{1}{3} \left(\tau_1 - \frac{1}{2} \right) \quad (7)$$

as in the ordinary LBE models. The number density of the second component satisfy the following diffusion equation [24]:

$$\frac{\partial n_2}{\partial t} + \nabla \cdot (n_2 \mathbf{u}) = \nabla \cdot (\mathcal{D} \nabla n_2). \quad (8)$$

The temperature field θ can be simulated by the density field n_2 . When the compressibility is negligible as in the small Mach number limit, the velocity field is approximately divergence-free and the temperature field satisfies the following “passive-scalar” equation:

$$\frac{\partial \theta}{\partial t} + \mathbf{u} \cdot \nabla \theta = \nabla \cdot (\mathcal{D} \nabla \theta), \quad (9)$$

where the diffusivity, \mathcal{D} , is given by

$$\mathcal{D} = \frac{1}{3} \left[\tau_2 (1 + 9\mathcal{G}_{22} \psi_2 d\psi_2/dn_2) - \frac{1}{2} \right]. \quad (10)$$

The diffusivity can be tuned independently of the viscosity by changing either τ_2 or the interaction strength, \mathcal{G}_{22} . For simplicity, \mathcal{G}_{22} is also set to zero in the present simulation. The LBE model is a much simplified version of that in [10] since no interparticle interaction is used.

B. Simulation of the Rayleigh-Bénard convection

In the most common form of RBC, a thin layer of viscous fluid is confined between two horizontal rigid boundaries maintained at different temperatures. When the fluid has a positive thermal expansion coefficient, and the gravity is in the same direction of the temperature gradient, the net buoyancy force is in the opposite direction of the gravity. As the temperature difference between the two boundaries is raised above a certain threshold, the static conductive state becomes unstable, and convection occurs abruptly.

The well-known Boussinesq approximation is often used in the study of natural convection. With this approximation, the material properties are assumed to be independent of temperature except in the body force term, where the fluid density ρ is assumed to be a linear function of the temperature, namely $\rho/\rho_\infty = 1 + \beta(T - T_\infty)$. Here ρ_∞ and T_∞ are the density and temperature at the reference point, and β the constant thermal expansion coefficient. The gravitational force is therefore $\rho_\infty \mathbf{g} + \rho_\infty \mathbf{g} \beta (T - T_\infty)$. After absorbing the first term into the pressure, the effective body force is linearly proportional to the temperature variation.

The Boussinesq equation can be simulated with the two-component LBE model by making the external gravitational acceleration, \mathbf{g} , in Eq. (6) a linear function of the temperature θ , *i.e.*,

$\mathbf{g} = -g\theta\mathbf{e}_z$, where \mathbf{e}_z is the unit vector in the vertical direction and g a parameter controlling the strength of the force. In Cartesian coordinates (x, y, z) , the lattices are of the sizes $L_x \times L_z$ and $L_x \times L_y \times L_z$ in 2D and 3D respectively. Periodic boundary condition is used in x and y directions, and the following no-slip, isothermal boundary condition is used in z direction:

$$\begin{cases} \mathbf{u} = 0, \theta = 0 & z = 0; \\ \mathbf{u} = 0, \theta = 1 & z = L_z. \end{cases} \quad (11)$$

Since the LBE fluid is always compressible, an externally applied force will cause a density variation. This compressible effect can be eliminated by absorbing into the pressure term the part of the body force that corresponding to the body force in the static conductive state, yielding the following net external acceleration

$$\mathbf{g} = -g \left(\theta - \frac{z}{L_z} \right) \mathbf{e}_z. \quad (12)$$

In the conductive state the above external force vanishes and the density field is homogeneous.

For a given the system size, the characteristic velocity, the Grashof number, the Rayleigh number and the Prandtl number are determined by the three parameters τ_1 , τ_2 and g in the LBE model as the following:

$$v_c = \sqrt{gL_z}, \quad Gr = \frac{gL_z^3}{\nu^2}, \quad R = GrPr = \frac{gL_z^3}{\nu\mathcal{D}}, \quad Pr = \frac{\nu}{\mathcal{D}} = \frac{2\tau_1 - 1}{2\tau_2 - 1}. \quad (13)$$

The Prandtl number is determined by the two relaxation times used for the two components. Given the two basic characteristic dimensionless numbers Pr and R , there is an extra degree of freedom in determining τ_1 , τ_2 and g . However, to ensure that the Mach number is small, v_c has to be kept small. Once v_c is chosen, all the parameters in the LBE model are determined by the two dimensionless numbers R and Pr .

C. Implementation of the boundary conditions

To implement the isothermal, no-slip boundary condition, we must ensure that at the boundary, the component simulating the fluid flow has zero velocity, and the component simulating

the temperature field has fixed density. The mass flux of the second component represents the heat transport through the boundaries. Usually the LGA and LBE methods implement the no-slip boundary condition by reversing the direction of the incoming particles at the boundary, yielding zero averaged velocity. This simple “bounce-back” method was found to be inaccurate [25,26]. In the present work, it results in errors of up to 50% in the critical Rayleigh number. More accurate and general methods have been developed to implement velocity boundary conditions in complex geometry [27–29]. These methods usually involve additional computation at the boundary sites. Here, because the boundaries are flat planes, both the velocity and the density boundary conditions can be implemented more efficiently.

When analyzing various implementations of boundary conditions, exact solutions in some simple cases are found to be very useful [28,30]. For simplicity, we consider the time-independent one-dimensional situation. All variables depend only on z , the coordinate perpendicular to the wall, so that the spatial dependence can be noted by a single superscript, j , starting from 0 at the lower boundary. The elements of the distribution functions n_a^j can be classified into three groups, n_+^j , n_-^j and n_0^j , according to the sign of $\mathbf{e}_a \cdot \mathbf{e}_z$. Eq. (1) reduces to the following simple form:

$$n_{\pm}^{j\pm 1} - n_{\pm}^j = -\frac{1}{\tau} [n_{\pm}^j - n_{\pm}^{j(\text{eq})}] \quad \text{and} \quad n_0^j = n_0^{j(\text{eq})}. \quad (14)$$

We assume the distribution functions at all sites including the boundary sites are updated uniformly using Eqs. (14). At the lower boundary sites, the groups n_+^0 and n_0^0 are unspecified. The only available information about the bulk of the fluid is n_-^0 , from which, n_+^1 is to be constructed according to some updating scheme so that certain hydrodynamic boundary condition is satisfied at macroscopic level. The “bounce-back” scheme simply sets $n_a^1 = n_b^0$ for any a and b satisfying $\mathbf{e}_a = -\mathbf{e}_b$. Obviously this in general does not satisfy Eqs. (14) with $\mathbf{u} = 0$ at the boundary. However, if we use the “bounce-back” scheme to calculate the group n_+^0 , namely we set $n_a^0 = n_b^0$ for any a and b satisfying $\mathbf{e}_a = -\mathbf{e}_b$, and calculating n_+^1 using Eqs. (14) with $\mathbf{u} = 0$ and $n = 6 \sum n_-^0$ in the computation of $n_+^{0(\text{eq})}$, the no-slip boundary condition will be satisfied. Here the summation is over all the elements in the group.

The isothermal boundary condition is imposed by fixing the density of the second component

at specified values on the boundaries. In the time-independent one-dimensional situation, the density profile of the passively convected component can be exactly solved from Eqs. (14). We sum all the elements of the distribution in each of the groups and note the sum as $N_{\pm}^j = \sum n_{\pm}^j$. By summing Eqs. (14) we find

$$N_{\pm}^{j\pm 1} - N_{\pm}^j = -\frac{1}{\tau} [N_{\pm}^j - N_{\pm}^{j(\text{eq})}] \quad (15)$$

Using Eq. (2) and notice that the velocity only has component parallel to the wall, we can find easily that $N_{\pm}^{j(\text{eq})} = n^j/6$, independent of the local velocity. Here n^j is the density at the j -th position. From the second part of Eq. (14), we have $N_+^j + N_-^j = n^j/3$. For any three consecutive j values, there are total of seven equations relating the six variables N_{\pm}^j to the three density values. On eliminating N_{\pm}^j from the seven equations, we find $2n^j = n^{j-1} + n^{j+1}$; namely, the density profile is linear in z as the diffusion equation predicts.

At the boundary sites, we must have

$$N_+^0 = N^0/3 - N_-^0. \quad (16)$$

In the computation, the isothermal boundary condition is implemented by computing the distribution function elements in the group n_+^0 according to the following equation:

$$n_a^0 = 2w_a n - n_b^0, \quad (17)$$

and then updating it using Eq. (1). Here a and b are any pair of indices such that e_a and e_b are mirror images of each other with respect to the boundary. In addition to satisfying Eq. (16), this scheme is also compatible with the no-slip boundary condition.

III. SIMULATION RESULTS

We present the simulation results in this section. The two basic characteristic dimensionless numbers are the Rayleigh number R and the Prandtl number Pr . The velocity and time reported hereafter are in the units of v_c and the characteristic time, L_z/v_c , respectively. The diffusion time $t_d = L_z^2/\mathcal{D}$ is \sqrt{PrR} in these units.

A. Onset of Rayleigh-Bénard instability

The critical Rayleigh number at which the static conductive state becomes unstable was given by the linear stability theory and confirmed by laboratory observations. The static conductive state is found to first become unstable to the disturbance of the wave number $k_c = 3.117$ in the x - y plane when the Rayleigh number exceeds the critical value of $R_c = 1707.762$. If the deviation from the Boussinesq approximation is small, the convection occurs in the form of two-dimensional rolls. Since the development of the instability is very slow at near-critical Rayleigh numbers, the computation has to be carried out for a long time before stable convection is fully developed. Because the first unstable disturbance is two-dimensional, we conduct the near-critical simulations primarily in 2D to save CPU time. The results were compared with 3D simulation results for some typical cases.

With periodic boundary condition, the wave number in x - y plane can only take discretized values given by

$$\left(\frac{k}{2\pi L_z}\right)^2 = \left(\frac{n_x}{L_x}\right)^2 + \left(\frac{n_y}{L_y}\right)^2, \quad n_x, n_y = 0, 1, 2, \dots \quad (18)$$

In 2D, the aspect ratio L_x/L_z has to be a multiplication of $2\pi/k_c$ to accommodate the disturbance of the wave number k_c . Of course this can only be satisfied approximately on a uniform lattice. In the near-critical computation, unless otherwise specified, we chose $L_x \simeq 2\pi L_z/k_c$ to save computation cost.

To measure the critical Rayleigh number, computations were started from the static conductive state at several different Rayleigh numbers close to R_c . An initial small perturbation was applied to the density field. The growth rates of the disturbance were then measured and extrapolated to obtain the Rayleigh number corresponding to zero growth rate.

Shown in Fig. 1 are the typical time-histories of the maximum velocities in z direction for three slightly-above-critical Rayleigh numbers of 1720, 1735 and 1750 respectively. The other parameters are $Pr = 1$, $\tau_1 = 1$, and $L_z = 50$ for all three runs. The peak velocity is found to grow exponentially and then saturate at a finite amplitude. The steady-state isotherms and the velocity

field are shown in Fig. 2 for the simulation with $R = 1750$. The growth rates were measured with least-square fitting in the exponential growth stage. The fitting results are shown as the straight lines.

The measured growth rates were plotted against the Rayleigh number in Fig. 3. Three sets of simulations with $\tau_1 = 0.55, 1.,$ and 1.5 were performed to investigate the accuracy of using different values of τ_1 . All other parameters were the same in these simulations. A solid straight line is fitted through the data points for each set of data. The intersections of the lines with the x -axis give the Rayleigh numbers corresponding to neutral stability. It is to be seen that near the critical Rayleigh number, using a τ_1 other than unity tends to change the growth rates, which causes an error in the prediction of the critical Rayleigh number.

We have also measured the critical Rayleigh number for different Prandtl numbers and with different system sizes. The measurement results and the parameters used are summarized in Table I. The biggest error seems to have been caused by using a large τ value in the computation. Fortunately, this does not impose a significant limitation on the range of physical parameters that can be simulated, because for a given Rayleigh number, τ_1 and τ_2 can always be kept small by using a small g .

Shown in the first part of Table I are five otherwise identical runs with different system sizes. The time history of the peak vertical velocity in these runs are plotted in Fig. 4. In the plot, the starting times were adjusted so that the initial perturbation levels are the same for all five runs. It can be seen that the convergence is fast and differences between the runs with $L_z > 20$ is insignificant.

Also shown in Fig. 4 is the result of a 3D simulation on a $128 \times 128 \times 32$ lattice with the same parameters. The growth rate in the early stage is the same as that in the 2D simulations. However, the peak velocity over-shoots before it saturates at the same level. Figs. 5 display a series of snapshots of the temperature distribution on a x - y plane laying in the middle between the two walls at the times $t = 1047, 1320, 1524$ and 2273 . The grey scales from the darkest to the brightest represents the temperature in the range $0.403 < \theta < 0.597$. The instability starts in the form of an array of convection cells, the superposition of the most unstable mode ($k = k_c$)

oriented in the x and y directions, and reaches its maximum near $t = 1320$ (Fig. 5b). The fully developed convection rolls oriented in one direction seem to suppress the orthogonal rolls and the final convection pattern is purely two-dimensional (Fig. 5d).

B. Higher Rayleigh number

The two-dimensional convection pattern characterized by the rolls is unstable at higher Rayleigh number. As the Rayleigh number is being increased, a series of transitions to more complicated states occur, and the form of the convection becomes both three dimensional and time-dependent, and eventually turbulent at very high Rayleigh number. Detailed numerical simulation of all the complicated transitions and the different forms of convection requires a large amount of computation. This is because the form of the convection depends on both the initial condition and the boundary conditions. A large number of runs have to be performed to cover the parameter space. In addition, the computation has to be carried out for a long time due to the large differences among the time scales in the problem. Here we only present the simulation results for a few typical situations at moderate Rayleigh numbers due to the limitation of computer resources.

A two-dimensional simulation at high Rayleigh numbers was performed on a 101×50 lattice with a Prandtl number of 0.71. The simulation was started from the static conductive state, beginning with $R = 2,000$. After the steady-state was reached, the Rayleigh number was raised step by step to higher values. The Nusselt numbers measured at the steady states are plotted in Fig. 6 against the Rayleigh number. The simulation results of Clever and Busse [31] are also plotted for comparison. Agreement is found at Rayleigh numbers less than 20,000. At higher Rayleigh numbers, the LBE simulation has a lower heat transport. We have raised the Rayleigh number to values as high as 10^6 for the same resolution. Unlike the thermal LBE model [15], the present model remains numerically stable.

Shown in Figs. 7 are the steady-state isotherms for some typical Rayleigh numbers. As the Rayleigh number is increased, the temperature gradient near the boundary becomes sharper; the ascending and descending fluid sheets become narrower, and the area in the interior of the fluid

with a reversed temperature gradient becomes wider.

The steady-state solutions were obtained by raising the Rayleigh number gradually after the convection roll has established at lower Rayleigh number. It was found however that if the simulation is started from the static conductive state with $R = 50,000$, the system will evolve into an oscillatory state. The dominant wavelength is half of that in the steady states solutions shown in Figs. 7, and the ascending and descending fluid sheets swing back and forth with a period of $0.174L_z/v_c$. The isotherms at the beginning, the quarter, the half and three quarters of one oscillation period are shown in Fig. 8. This oscillation does not occur in simulations with $R \leq 30,000$.

Three dimensional simulations were performed for the same Prandtl number and Rayleigh numbers on a $128 \times 128 \times 32$ lattice. Again, the computation was started from the static state with $R = 6,000$. Shown in Fig. 9 is the time history of the Nusselt number as the Rayleigh number was raised step by step to the values shown on the top of the graph. Greyscale plots of temperature distributions on the mid-plane at some typical times for different Rayleigh numbers are shown in Figs. 10. The 2D convection rolls have already exhibited some wavy instability at $R = 6,000$. However, the amplitude of the oscillation is so small that the deformation of the convection rolls is difficult to be detected from the static plots. To reveal the details of the oscillation, the scale has been enlarged and the time history of the Nusselt number replotted in this section. The slow decay of the amplitude of the oscillation might be an indication that in agreement with other workers [31,32], the Rayleigh number of 6,000 is very close to the threshold at which the convection becomes time-dependent. The evolution of the convection pattern became more and more complicated and oscillations of more frequencies were involves as the Rayleigh number was increased. At $R = 30,000$ and $50,000$, although the time history of the Nusselt number appeared to be quite chaotic, the temperature field plotted in Figs. 10 still posses rather regular structures and patterns. Simulations at higher Rayleigh number would require higher resolution. A detailed investigation of the transitions in RBC as the Rayleigh number is increased requires large number of runs and is certainly beyond the scope of the present work.

IV. CONCLUSIONS AND DISCUSSIONS

In this paper, we presented a method of simulating temperature evolution in fluid systems using multiple component LBE model. By simulating the temperature field using an additional component, we are able to avoid the numerical instability plaguing the thermal LBE models. The algorithm is simple, and the requirement on computational resources is twice of that for a non-thermal LBE code. As an example, we studied the Rayleigh-Bénard convection using this method. The results agree very well with theoretical predictions and experimental observations both at near-critical and moderate Rayleigh numbers.

The density of the additional component satisfies a passive-scalar equation. In the simulation of the Boussinesq equations, the external force is made to be a linear function of this passive scalar. However, this passive-scalar can represent other properties of the fluid satisfying more complicated equations. More importantly, when the equation of state is coupled with this passive scalar, the dynamic process of phase transition can be simulated. We defer the discussion of the details to a future publication.

ACKNOWLEDGMENTS

The author is grateful to Drs. Francis Alexander, Gary Doolen, Nicos Martys, David Montgomery, Joel Mozer, Rodney Worthing and Jeffrey Yopez for helpful discussions. The computation was performed using the resources of the Advanced Computing Laboratory at Los Alamos National Laboratory, Los Alamos, NM 87545.

REFERENCES

- [1] U. Frisch, B. Hasslacher, and Y. Pomeau, *Phys. Rev. Lett.* **56**, 1505 (1986).
- [2] S. Wolfram, *J. Stat. Phys.* **45**, 471 (1986).
- [3] G. R. McNamara and G. Zanetti, *Phys. Rev. Lett.* **61**, 2332 (1988).
- [4] P. L. Bhatnagar, E. P. Gross, and M. Krook, *Phys. Rev.* **94**, 511 (1954).
- [5] H. Chen, S. Chen, and W. H. Matthaeus, *Phys. Rev. A* **45**, R5339 (1992).
- [6] Y. H. Qian, D. d’Humières, and P. Lallemand, *Europhys. Lett.* **17**, 479 (1992).
- [7] S. Chen, Z. Wang, X. Shan, and G. D. Doolen, *J. Stat. Phys.* **68**, 379 (1992).
- [8] D. O. Martínez, W. H. Matthaeus, S. Chen, and D. Montgomery, *Phys. Fluids* **6**, 1285 (1994).
- [9] S. Hou *et al.*, *J. Comp. Phys.* **118**, 329 (1995).
- [10] X. Shan and H. Chen, *Phys. Rev. E* **47**, 1815 (1993).
- [11] X. Shan and H. Chen, *Phys. Rev. E* **49**, 2941 (1994).
- [12] N. Martys and H. Chen, *Phys. Rev. E* **53**, 743 (1996).
- [13] F. J. Alexander, S. Chen, and J. D. Sterling, *Phys. Rev. E* **47**, R2249 (1993).
- [14] Y. Chen, H. Ohashi, and M. Akiyama, *Physics of Fluids* **7**, 2280 (1995).
- [15] G. R. McNamara, A. L. Garcia, and B. J. Alder, *J. Stat. Phys.* **81**, 395 (1995).
- [16] C. Burges and S. Zaleski, *Complex Systems* **1**, 31 (1987).
- [17] X. Shan and G. Doolen, *J. Stat. Phys.* **81**, 379 (1995).
- [18] F. H. Busse, in *Hydrodynamic instabilities and the transition to turbulence*, 2nd ed., edited by H. L. Swinney and J. P. Gollub (Springer-Verlag, Berlin, 1986), pp. 97–133.
- [19] J. A. Domaradzki and R. W. Metcalfe, *J. Fluid Mech.* **193**, 499 (1988).

- [20] F. Massaioli, S. Succi, and R. Benzi, *Euro. Phys. Lett* **21**, 3 (1993).
- [21] F. Massaioli, R. Benzi, S. Succi, and R. Tripicciono, *Euro. J. Fluids* **14**, 1 (1995).
- [22] E. D. Siggia, *Annu. Rev. Fluid Mech.* **26**, 137 (1994).
- [23] S. Chapman and T. G. Cowling, *The Mathematical Theory of Non-Uniform Gases*, 3rd ed. (Cambridge University Press, London, 1970).
- [24] X. Shan and G. Doolen, *Phys. Rev. E* **54**, 3614 (1996).
- [25] R. Cornubert, D. d’Humières, and D. Levermore, *Physica D* **47**, 241 (1991).
- [26] I. Ginzbourg and P. M. Adler, *J. Phys. II France* **4**, 191 (1994).
- [27] D. R. Noble, S. Chen, J. G. Georgiadis, and R. O. Buckius, *Phys. Fluids* **7**, 203 (1995).
- [28] Q. Zou, S. Hou, and G. Doolen, *J. Stat. Phys.* **81**, 319 (1995).
- [29] I. Ginzbourg and D. d’Humières, *J. Stat. Phys.* **84**, 927 (1995).
- [30] X. He, Q. Zou, L. Luo, and M. Dembo, LANL preprint (unpublished).
- [31] R. M. Clever and F. H. Busse, *J. Fluid Mech.* **65**, 625 (1974).
- [32] J. B. McLaughlin and S. A. Orszag, *J. Fluid Mech.* **122**, 123 (1982).

TABLES

TABLE I. Critical Rayleigh number obtained by extrapolating growth rate data at slightly supercritical

Rayleigh numbers.

Run #	L_y	Pr	τ_1	τ_2	R_c	Error
1	50	1	1	1	1707.11	0.04%
2	30	1	1	1	1706.96	0.05%
3	20	1	1	1	1706.87	0.05%
4	10	1	1	1	1716.96	0.54%
5	50	0.1	1	5.5	1715.75	0.47%
6	50	100	1	0.505	1707.21	0.03%
7	50	1	0.55	0.55	1713.84	0.36%
8	50	1	1.5	1.5	1688.49	1.13%

FIGURES

FIG. 1. Typical time-histories of the peak vertical velocity in 2D simulation during the onset of the instability. The Rayleigh numbers are slightly above R_c . Other parameters are: $Pr = 1$, $\tau_1 = 1$, and the system size is 101×50 . The solid straight lines are the drawn by least-square fitting, the slope of which gives the growth rates of the instability.

FIG. 2. Steady state isotherms and velocity field in a two-dimensional simulation with the Rayleigh number of 1750. The resolution is 101×50 .

FIG. 3. Growth rates of the instability are found to depend linearly on the Rayleigh number near R_c . The symbols are the results of measurement from the time history of the peak vertical velocity, and the straight lines are fitted through the data points. The exact critical Rayleigh number is obtained by extrapolating the data to the zero growth rate. Three sets of simulations with different values of τ_1 were performed to determine the effects of different τ_1 on the accuracy. The simulations were performed on a 2D 101×50 lattice and is for $Pr = 1$.

FIG. 4. Time histories of the peak vertical velocity for different system sizes. It is to be seen that the simulation results converge for system sizes $L_z > 20$. The peak velocity in the 3D simulation has the same growth during the early development of the instability and saturates at the same level. The 3D effects peak around $t = 1320$.

FIG. 5. Greyscale plot of temperature distribution on the mid-plane between the two walls at, (a) $t = 1047$, (b) $t = 1320$, (c) $t = 1524$ and (d) $t = 2273$. The gray scales from the darkest to the brightest are mapped to the temperature range $0.403 < \theta < 0.597$.

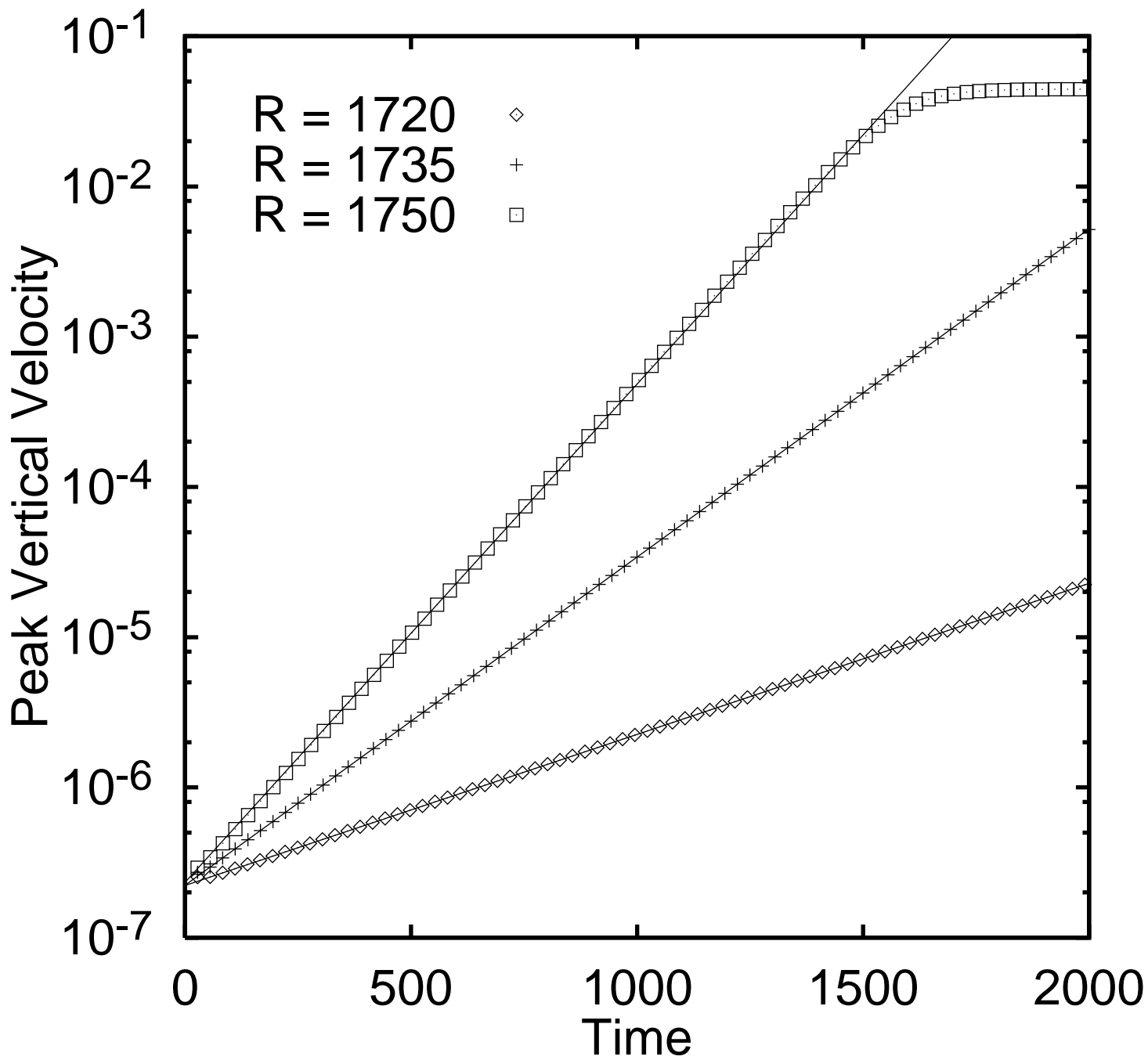
FIG. 6. The steady-state Nusselt number as function of the Rayleigh number in two-D simulations. The LBE results agree with that of Clever and Busse for Rayleigh number less than 20,000.

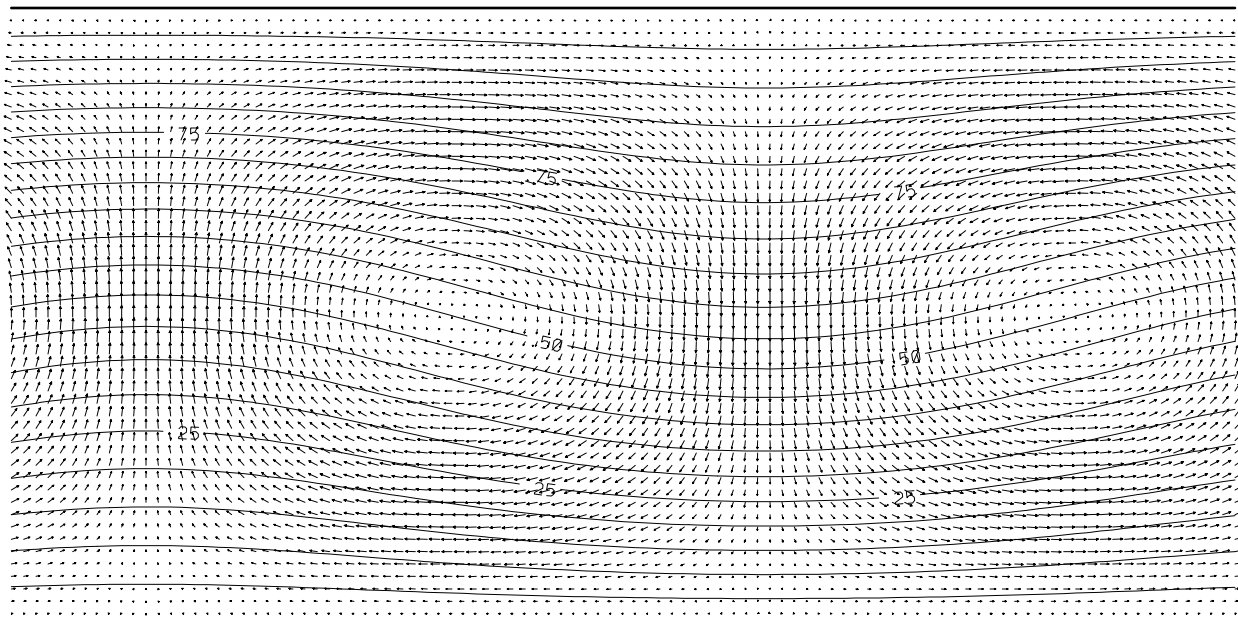
FIG. 7. Two-D simulation. Isotherms at steady states as the Rayleigh number is raised gradually to (a) 10,000, (b) 20,000, (c) 30,000 and (d) 50,000.

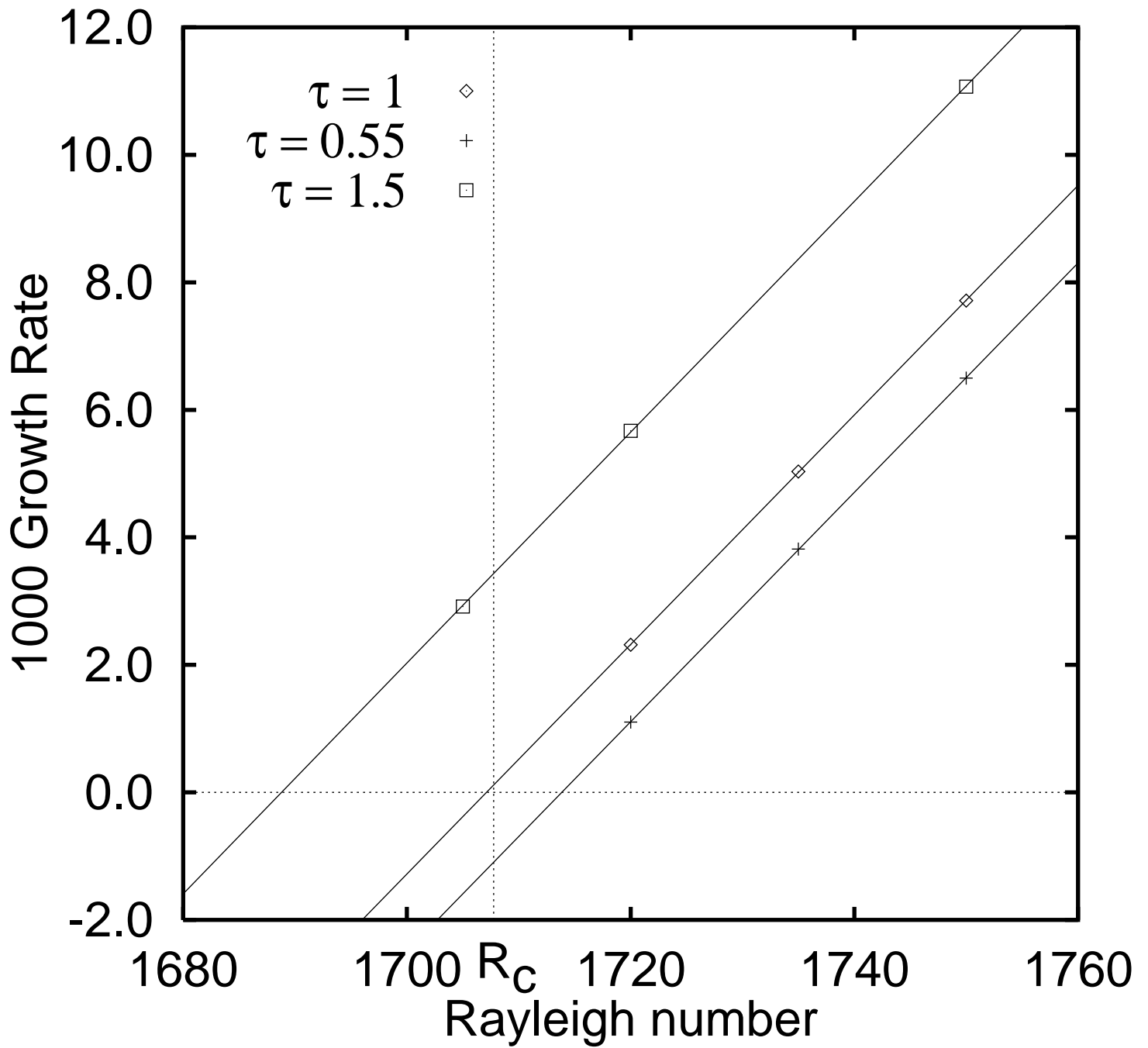
FIG. 8. Isotherms in two-D simulation. The simulation was started from the static conductive state with $R = 50,000$. The system evolves into a oscillatory state. The isotherms are taken at (a) the beginning, (b) one quarter, (c) half, and (d) three quarter of one oscillation period.

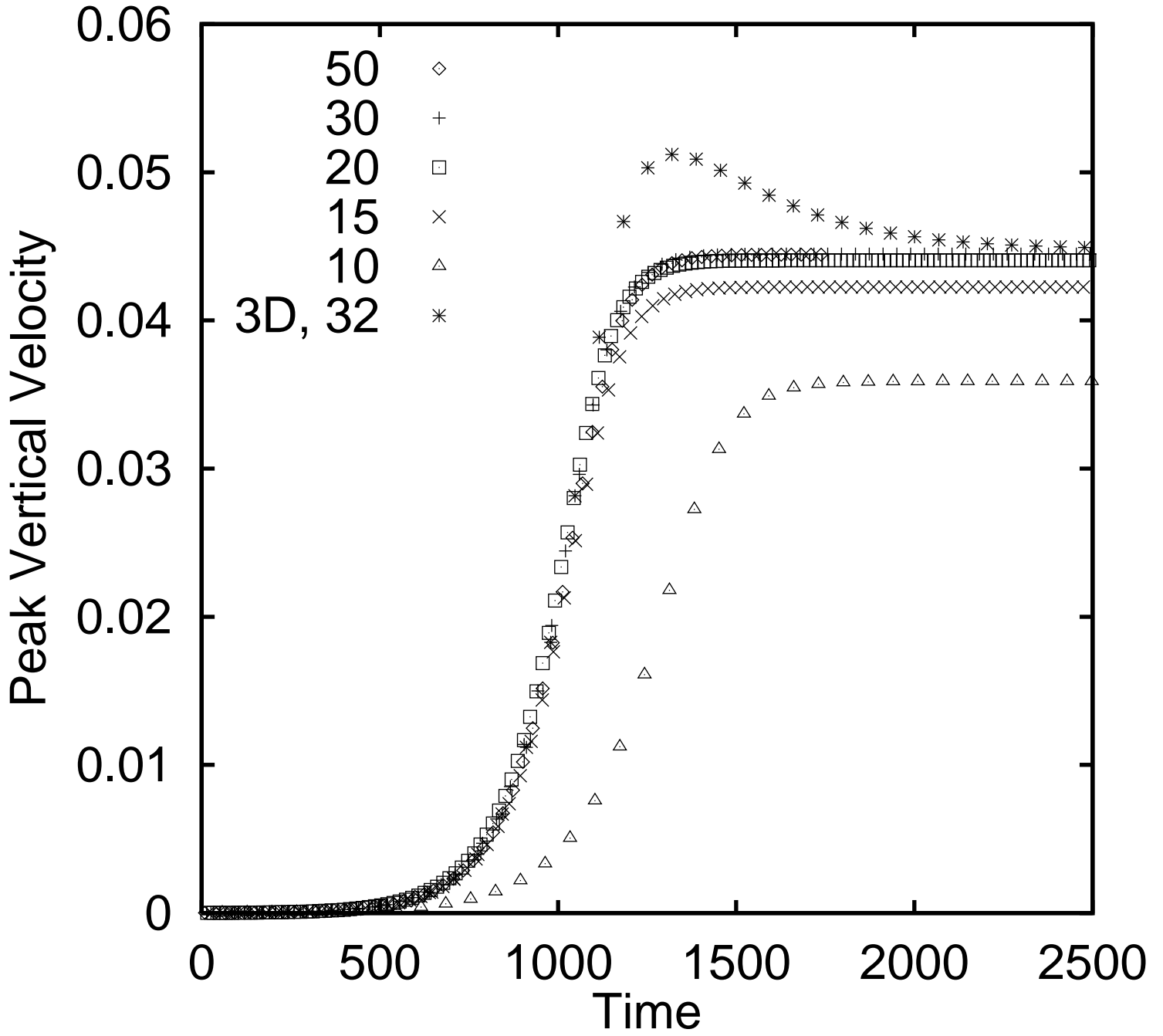
FIG. 9. Time history of the Nusselt number in a 3D simulation as the Rayleigh number is increased step by step at times indicated by the vertical dashed lines. For the first segment, the scale has been adjusted to the range of 2.08 to 2.082 and the Nusselt number replotted.

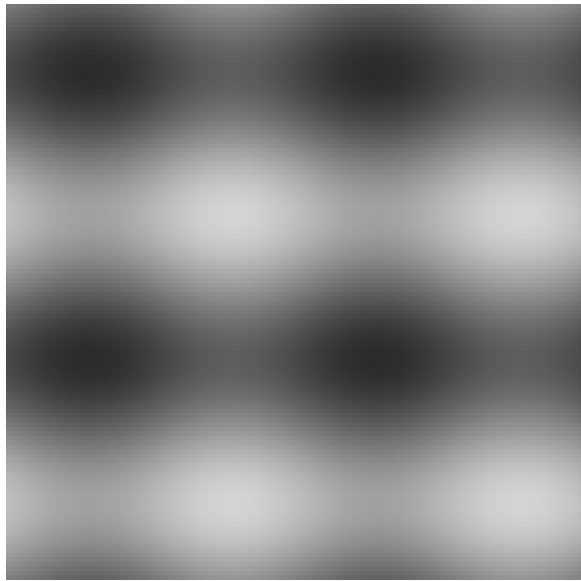
FIG. 10. Greyscale plots of typical temperature distribution on the mid-plane between the two walls for Rayleigh number (a) 6,000, (b) 8,000, (c) 10,000, (d) 20,000, (e) 30,000, and (f) 50,000.



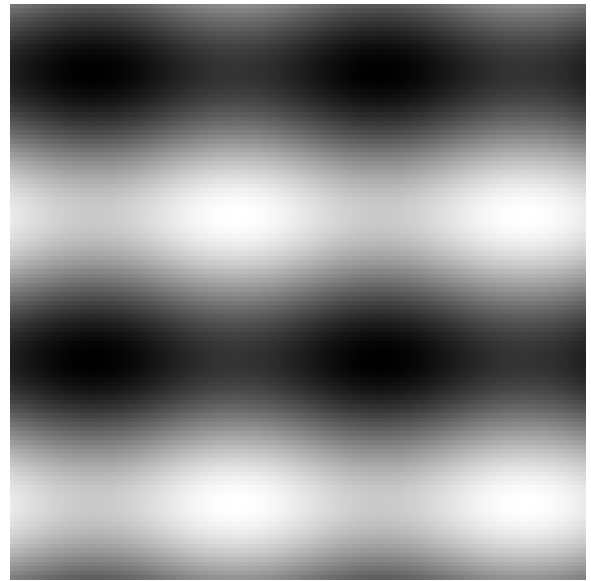




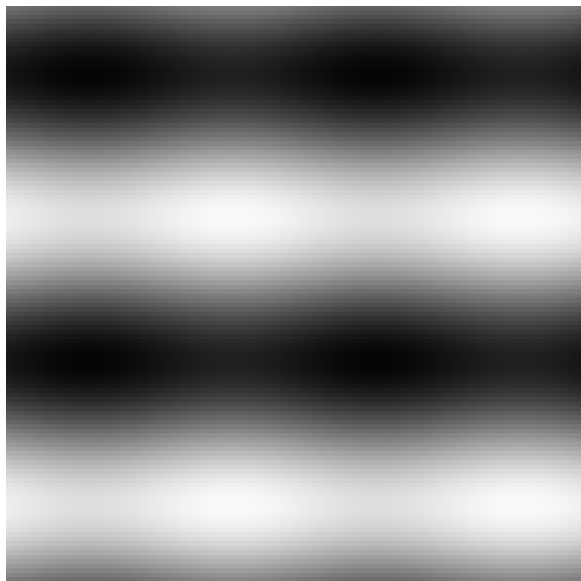




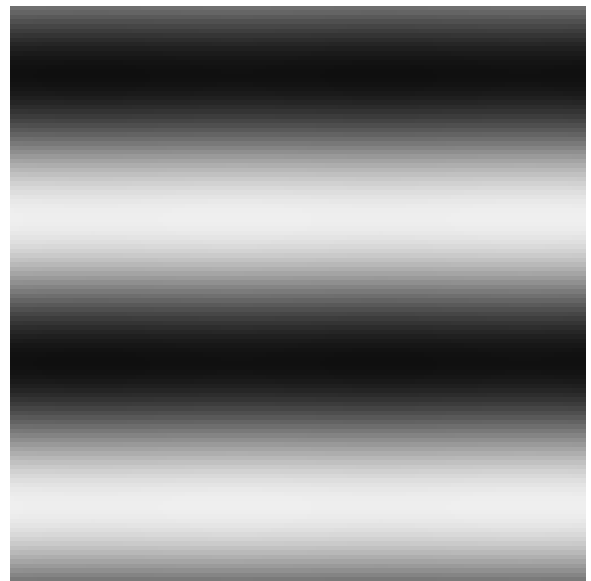
(a)



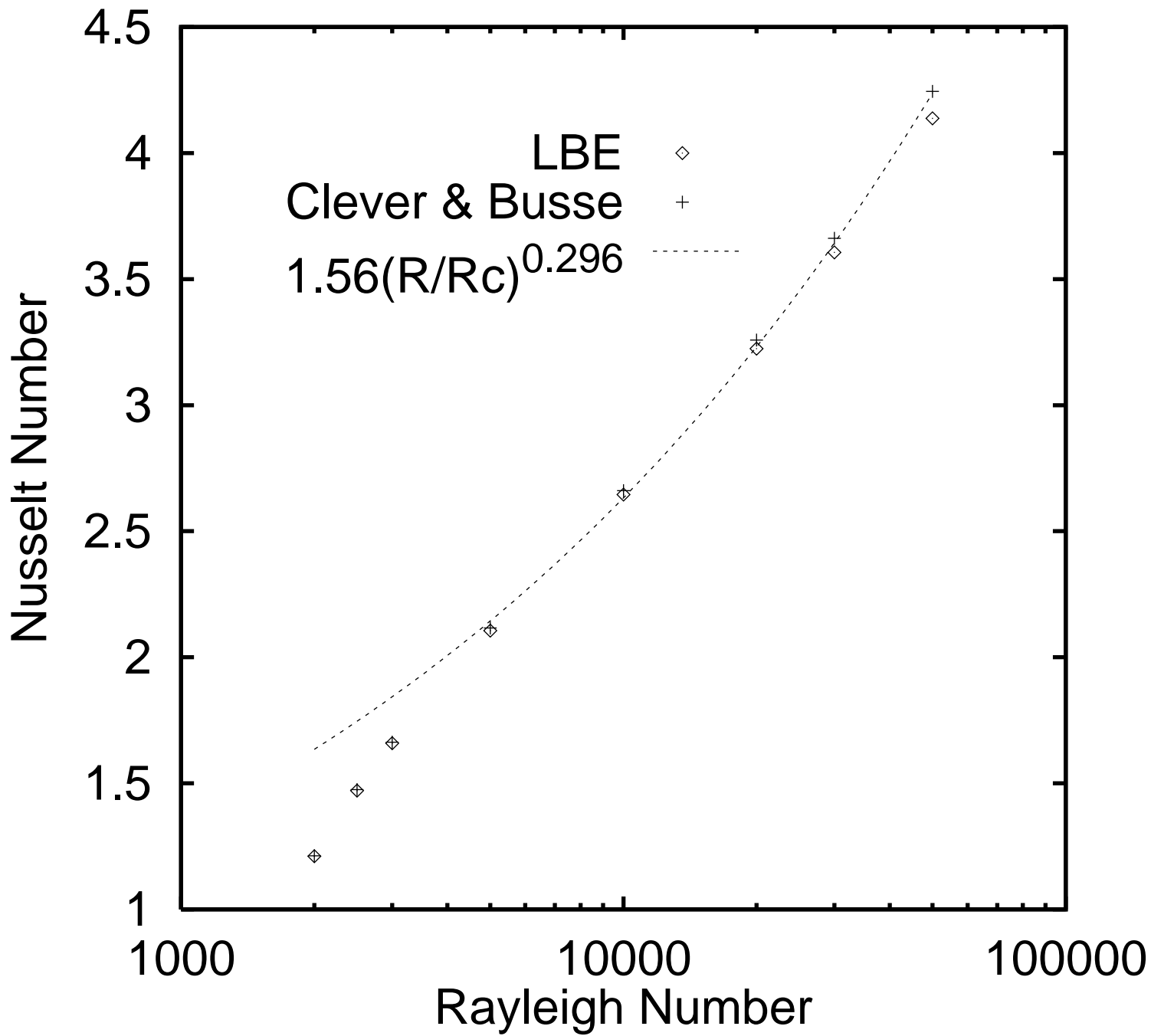
(b)

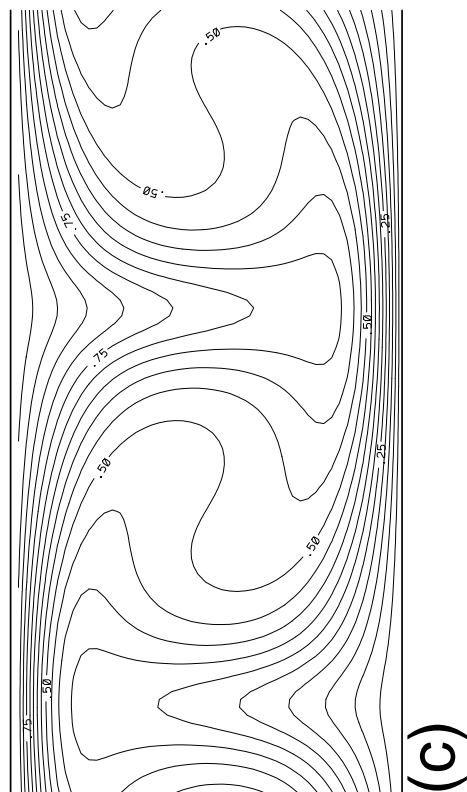
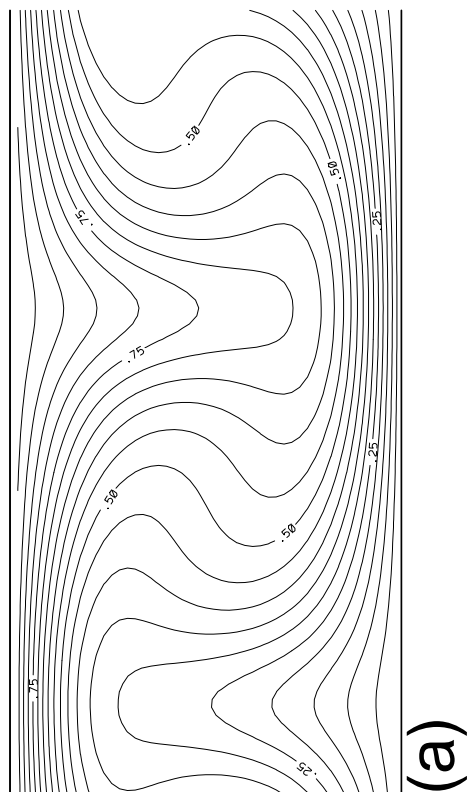
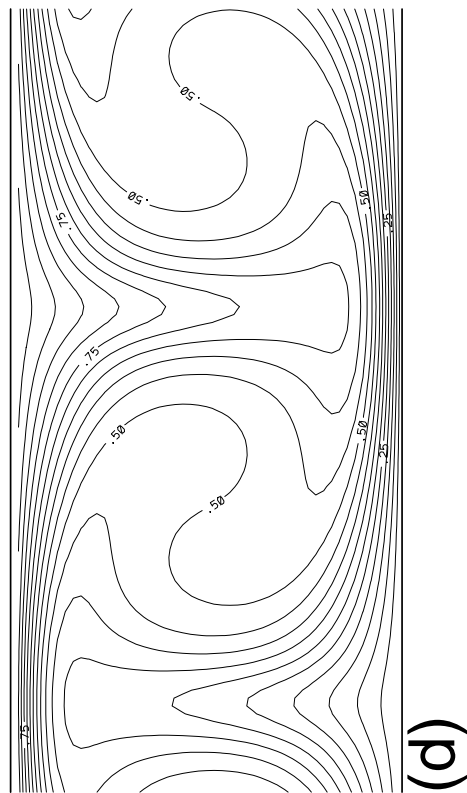
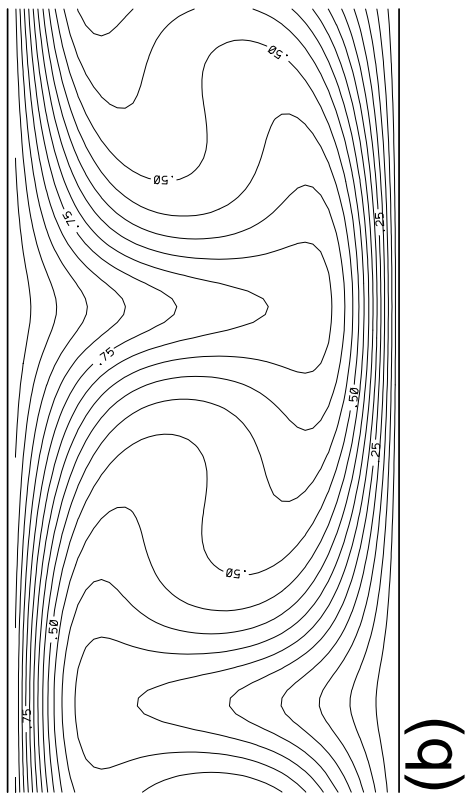


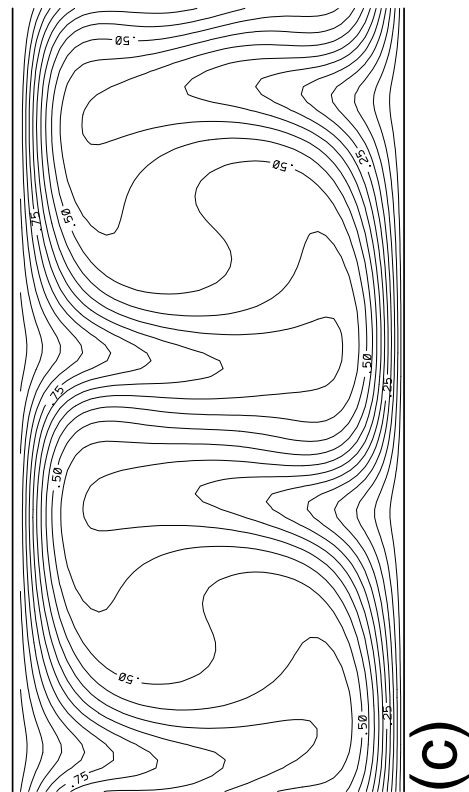
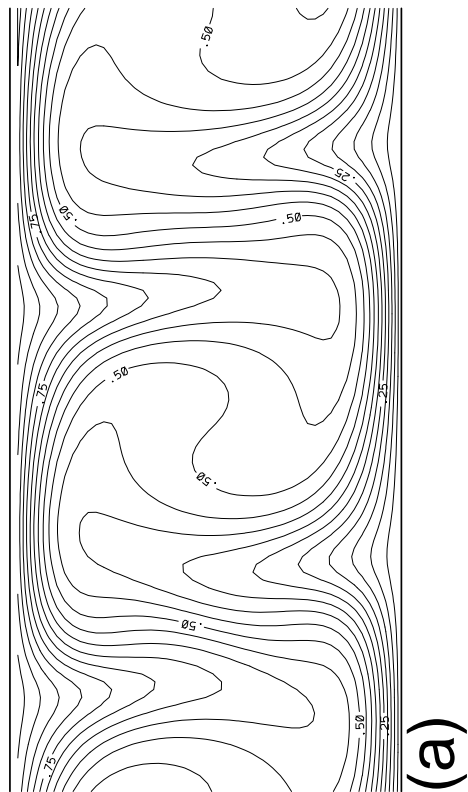
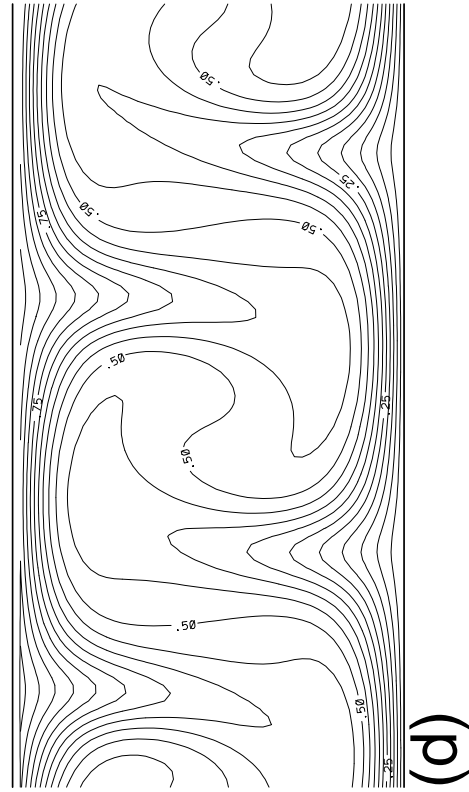
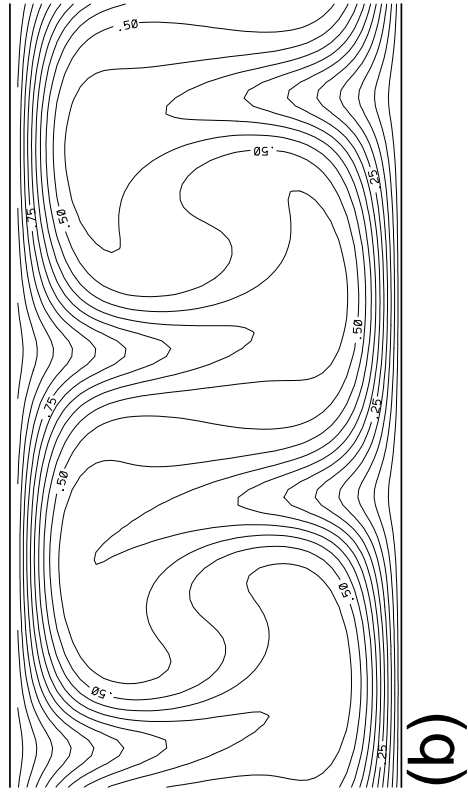
(c)

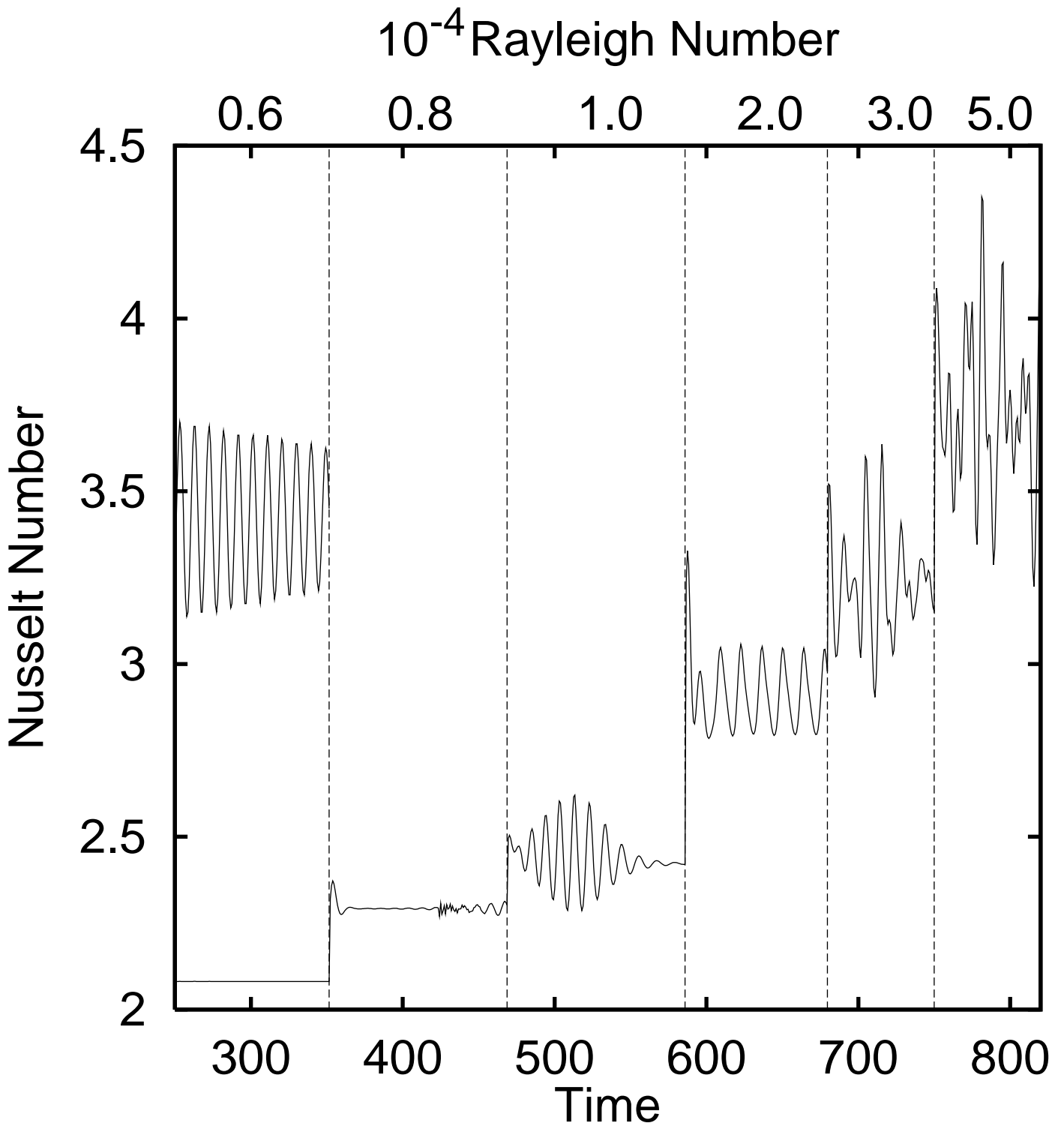


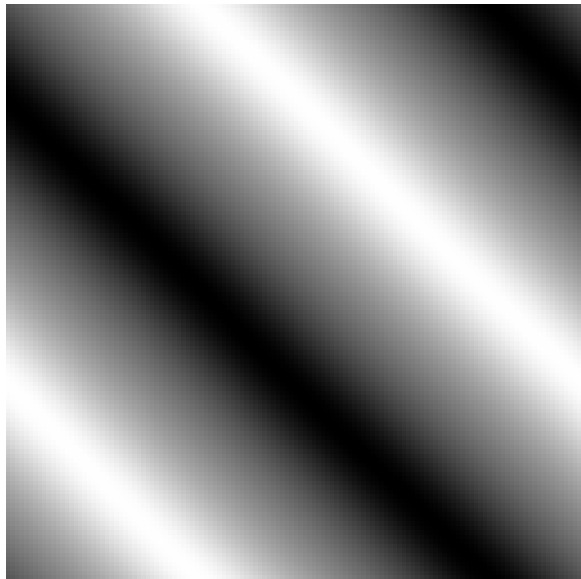
(d)



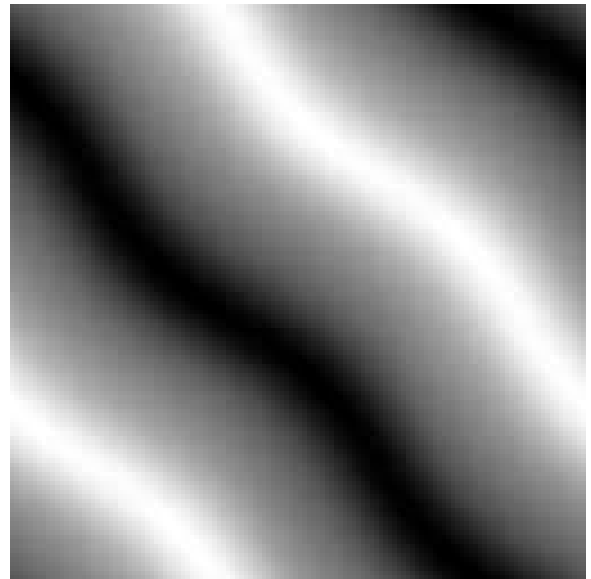




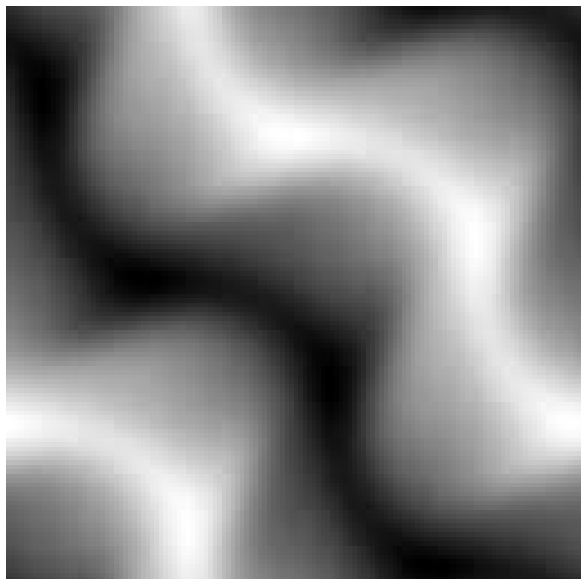




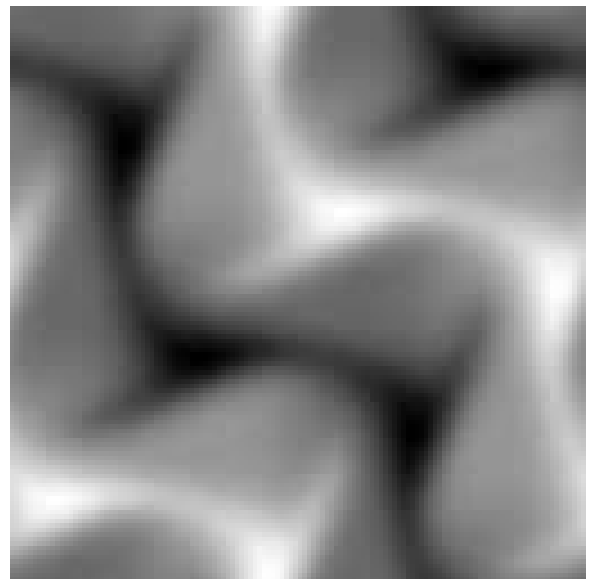
(a)



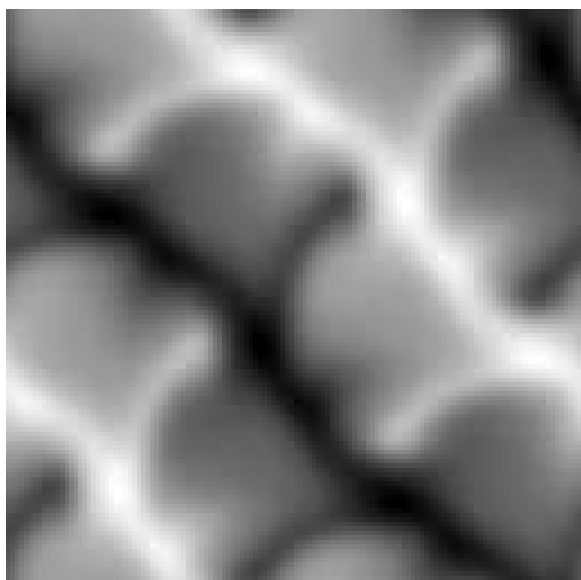
(b)



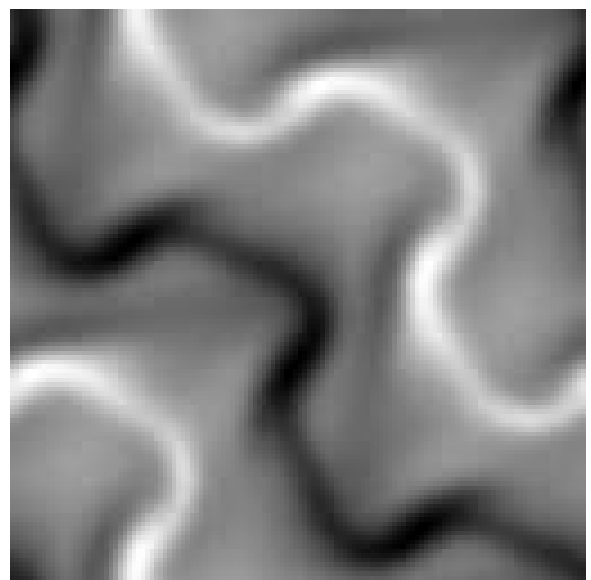
(c)



(d)



(e)



(f)